Published on 22 October 2025. Downloaded by Sungkyunkwan University on 2/3/2026 8:45:46 AM.

Nanoscale

ROYAL SOCIETY OF CHEMISTRY

PAPER

View Article Online
View Journal | View Issue

Cite this: *Nanoscale*, 2025, **17**, 24773

From N-type doping to phase transition in large-area MoS_2 *via* controlled sulfur vacancy formation

Jimin Kim,†[a] Jieun Kang,†[b] Hyewon Han,[a] Sunjae Jeong,[c] Siyeon Kim,[c] Heesoo Lee,[b] Hyoungsub Kim, [b] Yongil Kim*[d] and Geunyoung Yeom *[b]

Received 9th September 2025,
Accepted 15th October 2025

DOI: 10.1039/d5nr03806e

rsc.li/nanoscale

Precise and damage-free doping of two-dimensional semiconductors is essential for advancing their use in nano-electronic and optoelectronic devices. Here, we present a controllable strategy for n-type doping and phase engineering of monolayer MoS_2 by tuning sulfur vacancy formation using energy-controlled Ar^+ ion treatment. This method enables selective top-layer sulfur removal without disrupting the underlying lattice, leading to enhanced n-type conductivity. Extended plasma exposure induces a phase transition from the semiconducting 2H phase to the metallic 1T phase, as confirmed by Raman, photoluminescence, and X-ray photoelectron spectroscopy. Doped devices exhibit improved electrical and optoelectronic performance, including higher on-current, carrier mobility, and photoresponsivity. Additionally, selective formation of 1T contacts at the source/drain regions further reduces contact resistance and boosts injection efficiency. Al_2O_3 encapsulation is shown to suppress surface oxidation during O_2 plasma exposure, maintaining device stability. This work demonstrates that plasma-assisted defect and phase control offers a practical and scalable pathway to tailor the electronic properties of 2D semiconductors.

Introduction

Molybdenum disulfide (MoS_2), a two-dimensional transition metal dichalcogenide (2D TMD), has emerged as a key material for next-generation nano-electronic and optoelectronic devices due to its high field-effect mobility, tunable bandgap (~1.9 eV for monolayer and ~1.3 eV for bulk), and strong light–matter interaction.[1–4] In particular, MoS_2 synthesized by chemical vapor deposition (CVD) enables uniform fabrication over large areas, ensuring high compatibility with conventional semiconductor processes.[5–7] To apply these promising properties to practical devices, reliable and precise doping control is essential. Just as n-type and p-type doping are critical in silicon-based field-effect transistors (FETs), doping in TMD-based devices plays a central role in modulating carrier injections, contact resistance, and threshold voltage.[8,9] However, due to the atomic thickness and structural sensitivity of 2D materials, achieving stable and reproducible doping remains a significant challenge.[10]

Recently, defect engineering, which refers to the intentional introduction and control of atomic-scale defects, has gained attention as a promising strategy to achieve doping effects in MoS_2. MoS_2 is known to host a variety of defects such as point defects (*e.g.*, sulfur vacancies), anti-site defects, dislocations, and grain boundaries, all of which can significantly influence its electronic properties.[11–16] These defects can induce Fermi level pinning, reduce contact resistance, and even lead to phenomena such as band inversion and magnetism. However, randomly formed defects in MoS_2 can degrade device performance by transforming the material into a compensated semiconductor. Therefore, precise control over the type, density, and spatial distribution of defects is crucial.

To induce sulfur vacancies in MoS_2 for n-type doping, various approaches including chemical plasma treatments, thermal annealing, and solution-based methods have been applied.[17–19] However, these methods often suffer from critical limitations such as the use of toxic reagents, difficulty in controlling doping concentration due to time-sensitive transitions (*e.g.*, from n-type to p-type), and the requirement of high processing temperatures, which can cause thermal stress and interfacial diffusion. These factors may limit the stability and scalability of the process, especially for applications in flexible or thermally sensitive electronic platforms.

[a]*Department of Semiconductor Convergence Engineering, Sungkyunkwan University, Gyeonggi-do 16419, Republic of Korea*
[b]*Department of Advanced Materials Science & Engineering, Sungkyunkwan University, Gyeonggi-do 16419, Republic of Korea. E-mail: gyyeom@skku.edu*
[c]*Department of Display Engineering, Sungkyunkwan University, Gyeonggi-do 16419, Republic of Korea*
[d]*College of Information and Communication Engineering, Sungkyunkwan University, Gyeonggi-do 16419, Republic of Korea. E-mail: yikim11@skku.edu*
† These authors equally contributed to the work.

Published on 22 October 2025. Downloaded by Sungkyunkwan University on 2/3/2026 8:45:46 AM.

To overcome these limitations, we propose a room-temperature, low-damage, and chemically inert plasma-based defect engineering method for CVD-grown MoS_2. Using an ion beam etching (IBE) system with precisely controlled ion energy, we demonstrate the selective removal of only the top-layer sulfur atoms without damaging the underlying Mo lattice. Since the process involves only physical sputtering by inert Ar^+ ions without reactive gases, it avoids chemical damage or contamination of the MoS_2 surface. This allows the controlled formation of sulfur vacancies, enabling precise n-type doping, and, as the defect density increases, also facilitates a phase transition from semiconducting 2H to metallic 1T phase.[20]

These doping and phase transition processes were systematically analyzed using Raman spectroscopy and X-ray photoelectron spectroscopy (XPS) and further examined through structural and electrical characterizations using scanning transmission electron microscopy (STEM) and *I–V* measurements. The transfer characteristics obtained from the *I–V* characteristics confirmed significant improvements in device performance, including enhanced on/off ratio and carrier mobility. This study demonstrates that ion–assisted defect engineering using inert Ar gas offers a precise approach to modulate the electronic structure of MoS_2 and may serve as a promising platform for future high-performance 2D nano-electronic devices.

Results and discussion

A schematic illustration of the 3-grid ion beam extraction system used in this study is shown in Fig. 1a. The system consists of an inductively coupled plasma (ICP) source and a tri-grid structure for controlled ion acceleration. This configuration allows for precise tuning of the Ar^+ ion energy, enabling directional bombardment of the MoS_2 surface with minimal lattice disruption. Through energy-controlled ion exposure, selective removal of top-layer sulfur atoms can be achieved without damaging the underlying molybdenum or bottom sulfur atoms. The top-view atomic structure of monolayer MoS_2 before and after Ar^+ ion treatment is presented in Fig. 1b. In the untreated state, Mo and S atoms form a well-ordered hexagonal lattice. Upon exposure to Ar^+ ions, sulfur vacancies are generated predominantly at the top sulfur sites, while the Mo framework remains intact. The formation of these vacancies introduces donor-like defect states, effectively shifting the Fermi level and resulting in n-type doping behavior. This observation is consistent with previous reports demonstrating the electron-donating characteristics of sulfur vacancies in TMD materials.[11–19] A schematic process flow of n-type doping in MoS_2 *via* Ar^+ ion treatment is depicted in Fig. 1c. During the treatment, Ar^+ ions in the plasma selectively interact with the top-layer sulfur atoms, leading to their partial removal and the formation of controlled vacancy concentrations. The doping level can be modulated by adjusting the plasma exposure time. The created sulfur vacancies serve as electron donors, thereby enhancing the n-type conductivity of the MoS_2 channel. This controlled sulfur depletion strategy confirms the viability of defect engineering for tuning electronic properties in two-dimensional materials.

Fig. 2a shows the evolution of Raman spectra of a monolayer MoS_2 under varying Ar^+ ion treatment duration. From 20 to 90 seconds of ion exposure, the overall Raman peaks gradu-

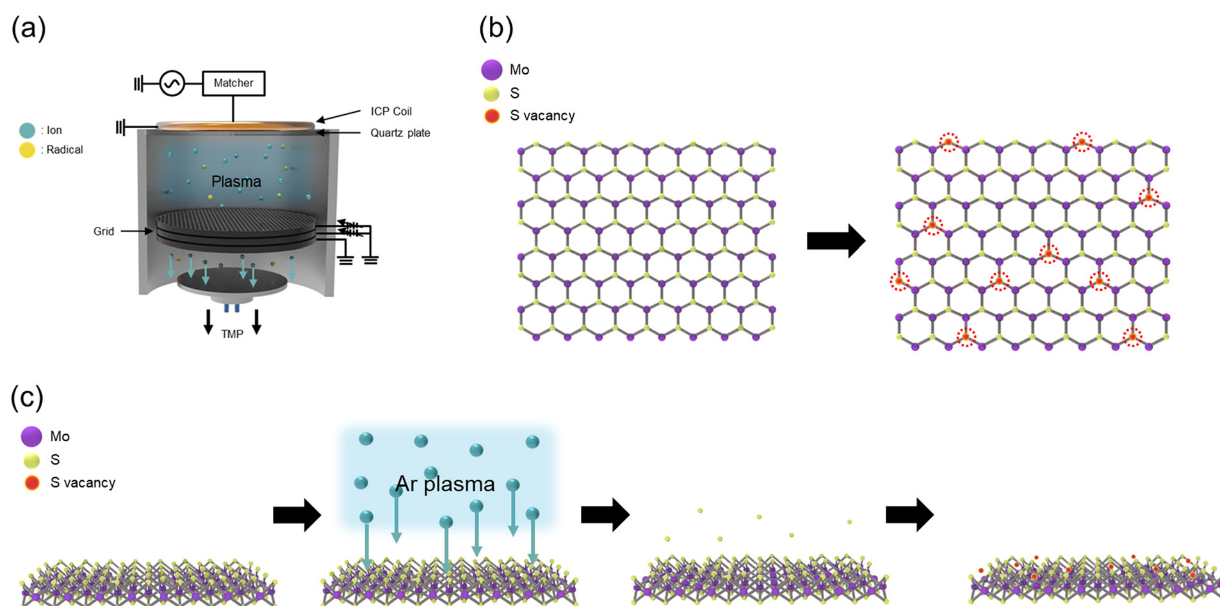

Fig. 1 Schematics and process flow of Ar^+ ion induced n-type doping in MoS_2. (a) Schematic illustration of the 3-grid ion beam system used for plasma generation. (b) Top-view schematic of the MoS_2 atomic structure before and after sulfur vacancy formation. (c) Process flow diagram of n-type doping in MoS_2 using Ar^+ ion treatment.

 This journal is © The Royal Society of Chemistry 2025

Published on 22 October 2025. Downloaded by Sungkyunkwan University on 2/3/2026 8:45:46 AM.

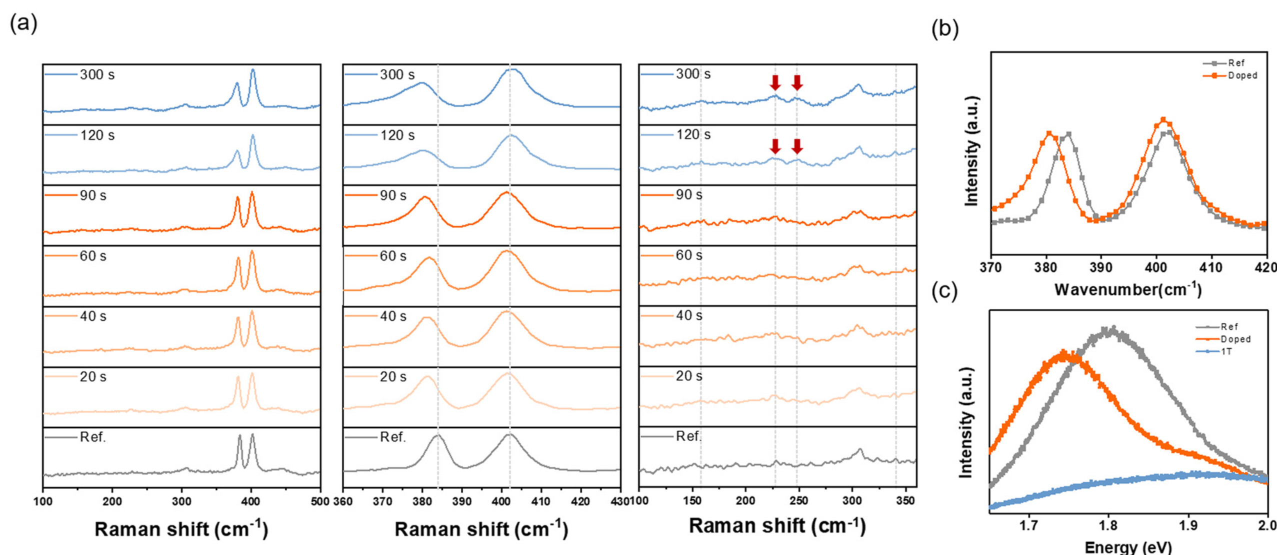

Fig. 2 Raman and photoluminescence (PL) characterizations of MoS_2 under varying Ar^+ ion treatment duration. (a) Evolution of Raman spectra of MoS_2 with increasing Ar^+ ion exposure time (0–300 s), showing shifts in peak positions and intensity changes over time. (b) Comparison of E_{2g} and A_{1g} Raman modes between the reference and doped MoS_2 samples (60 s Ar^+ ion exposure) indicating changes in vibrational characteristics due to doping. (c) Photoluminescence spectra of reference, doped (90 s Ar^+ ion exposure), and 1T-phase MoS_2 (300 s Ar^+ ion exposure) samples, showing a reduced PL intensity in the doped sample and further suppression in the 1T phase.

ally red-shift, which suggests slight modifications in the crystal structure, such as charge doping or the formation of minor lattice distortions. These changes reflect the initial stages of material alteration before any significant phase transition occurs.[21] When the plasma exposure time is extended to 120 and 300 seconds, the Raman peaks begin to blue-shift, indicating a structural transformation from the semiconducting 2H phase to the metallic 1T phase.[22,23] In addition, new Raman peaks appear in the 150–350 cm^{-1} range specifically at 120–300 seconds, which further supports the formation of distorted vibrational modes characteristic of the 1T phase—features that are absent in the pristine 2H lattice.[20,22,23] Fig. 2b provides a comparative analysis of the E_{2g} and A_{1g} Raman modes between the reference and doped sample (90 s Ar^+ ion exposure). The A_{1g} mode, associated with out-of-plane vibrations of sulfur atoms, exhibits red-shift and noticeable peak broadening in the doped sample. This behavior is attributed to increased free carrier concentration and enhanced electron–phonon coupling, consistent with electron doping.[24] In contrast, the E_{2g} mode, corresponding to in-plane vibrations of Mo and S atoms, undergoes a slight red-shift primarily due to increased lattice disorder and defect formation rather than doping.[24,25] These distinct responses of the two modes highlight their respective sensitivities to doping and structural defects. Fig. 2c presents the photoluminescence (PL) spectra of reference, doped (90 s Ar^+ ion exposure), and 1T-phase MoS_2 (300 s Ar^+ ion exposure) samples. The doped sample exhibits a red-shifted PL peak along with significantly quenched intensity, indicative of n-type doping and reduced radiative recombination due to excess free carriers.[26] For the 1T-phase sample, the PL signal is almost entirely suppressed, consistent with the loss of direct bandgap transitions in the metallic phase.[23]

Fig. 3a shows the XPS spectra of the Mo 3d and S 2p, and O 1s core levels in MoS_2 under varying Ar^+ ion treatment duration. As the exposure time increases up to 90 seconds, both the Mo $3d_{5/2}$ and S $2p_{3/2}$ peaks shift slightly toward higher binding energies, which is typically associated with increased electron density near Mo atoms, indicating n-type doping.[10,27,28] At longer exposure duration of 120–300 seconds, the peaks shift back to lower binding energies, suggesting changes in the electronic structure, such as a transition to the metallic 1T phase.[29] Fig. 3b presents the quantitative evolution of the binding energies. The Mo $3d_{5/2}$ peak reaches its highest energy at 90 seconds, while the S $2p_{3/2}$ peak gradually increases and then drops after extended exposure, implying an electron doping-dominant regime in the early stage, followed by structural phase transformation. This trend corresponds well with the results from Raman and PL spectroscopy in Fig. 2, which show peak shifts in the initial stage, and upon longer treatment, definitively confirm the phase transition through the emergence of new 1T-specific peaks (Fig. 2a) and the quenching of the photoluminescence signal (Fig. 2c). Fig. 3c illustrates the evolution of the S/Mo atomic ratio calculated from the XPS peak areas. This ratio steadily decreases with increasing ion treatment time, indicating the progressive depletion of sulfur atoms from the MoS_2 surface. With further treatment, the S/Mo ratio stabilizes; this plateau is attributed to a self-limiting etching process where the removal of the top sulfur layer exposes the more strongly-bound Mo layer, leading to a saturation of vacancy creation.[30] The observed initial sulfur loss is consistent with the formation of sulfur vacancies, which act as electron donors and are responsible for the n-type doping behavior. Subsequently, however, the high, saturated concentration of vacancies serves as the thermodynamic

Published on 22 October 2025. Downloaded by Sungkyunkwan University on 2/3/2026 8:45:46 AM.

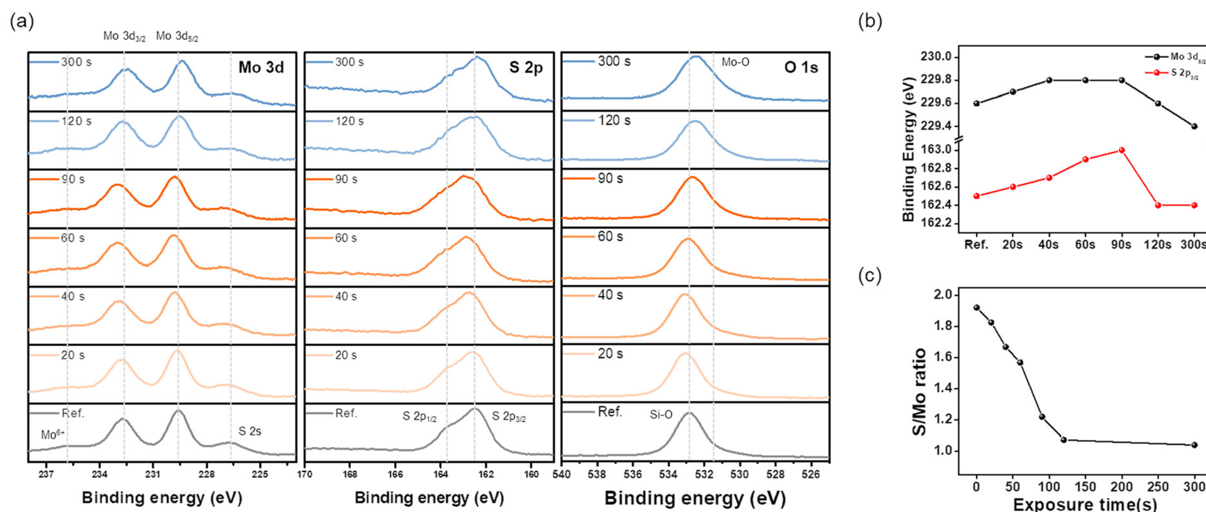

Fig. 3 XPS analysis of MoS_2 samples treated with Ar^+ ion for varying duration. (a) X-ray photoelectron spectroscopy (XPS) spectra showing the Mo 3d and S 2p, and O 1s core-level peaks of MoS_2 as a function of Ar^+ ion exposure time (0–300 s). (b) Binding energy shifts of the Mo $3d_{5/2}$ and S $2p_{3/2}$ peaks with increasing ion treatment time, indicating changes in the chemical environment due to sulfur vacancy formation. (c) Evolution of the S/Mo atomic ratio extracted from XPS spectra, showing a steady decrease with longer ion exposure duration.

driving force for the 2H-to-1T phase transition, as supported by a theoretical work showing that the 1T phase becomes energetically favorable beyond a critical vacancy concentration.[31] To address the potential for oxidation, the O 1s spectrum was also investigated (Fig. 3a). While no distinct Mo^{6+} peak is seen in the Mo 3d spectrum, a minor Mo–O peak in the O 1s spectrum suggests that the created sulfur vacancies are reactive sites susceptible to oxidation upon air exposure.[32] This inherent instability, which leads to long-term device degradation (Fig. S3), highlights the necessity of the protective encapsulation strategy that will be discussed in Fig. 6. Fig. 4 presents a comprehensive overview of the electrical, optoelectronic, and structural properties of a monolayer MoS_2 before and after the doping by Ar^+ ion treatment. In Fig. 4a, the transfer characteristics of MoS_2 field-effect transistors (FETs) show a noticeable increase in on-current with longer ion exposure, indicating enhanced channel conductivity due to electron doping. This trend is further supported by the linear-scale transfer curves presented in Fig. S1, where the progressive increase in current is clearly resolved. Additionally, the threshold voltage shifts progressively in the negative direction, which is a typical indicator of n-type doping induced by increased electron concentration in the channel.[9,10,17,19]

Fig. 4b and c display time-resolved photocurrent responses under periodic illumination with red (λ = 650 nm) and blue (λ = 450 nm) light, respectively. In both cases, the doped (90 s) devices exhibit a clear enhancement in photocurrent compared to the reference. The mechanism for this enhancement is attributed to the improved separation of photogenerated electron–hole pairs, facilitated by the Ar^+-induced sulfur vacancies. Sulfur vacancies can act as effective trapping centers for photogenerated holes, which suppresses carrier recombination and increases the lifetime of photogenerated electrons, thereby boosting the net photocurrent.[33] This is consistent with studies showing that a higher density of sulfur vacancies leads to an enhanced n-doping effect, which is directly correlated with a significant increase in photoresponse.[34] This improvement is further quantified in Fig. 4d, which shows that photoresponsivity increases significantly after doping (90 s) under both red and blue illumination. These results demonstrate that the doping by Ar^+ ion treatment not only improves the electrical transport properties of MoS_2 but also enhances its optoelectronic performance. Finally, Fig. 4e shows high-resolution STEM images of the pristine and doped (90 s) MoS_2 samples. In the doped sample, multiple sulfur vacancies—highlighted by red dashed circles—are clearly observed. These defects are directly linked to the doping mechanism and are considered the primary source of the observed electrical and optical changes. The atomic-scale structural transition accompanying vacancy formation is further detailed in Fig. S2, where high-resolution STEM imaging and intensity profiling confirm the transformation from the 2H to the 1T phase.

Fig. 5a compares the transfer characteristics of monolayer MoS_2 FETs fabricated with conventional 2H-phase contacts (reference) and with contact regions selectively converted to the 1T metallic phase. The 1T-contact device exhibits a significantly higher on-current, steeper subthreshold swing, and improved transfer characteristics, confirming that 1T phase engineering at the source/drain contacts effectively reduces contact resistance and enhances carrier injection efficiency. Fig. 5b shows the impact of n-type doping applied to the channel region. A significant negative shift in the threshold voltage is observed, which directly indicates a substantial increase in the electron concentration due to effective n-type doping by sulfur vacancies. While the on-state current also

 This journal is © The Royal Society of Chemistry 2025

Published on 22 October 2025. Downloaded by Sungkyunkwan University on 2/3/2026 8:45:46 AM.

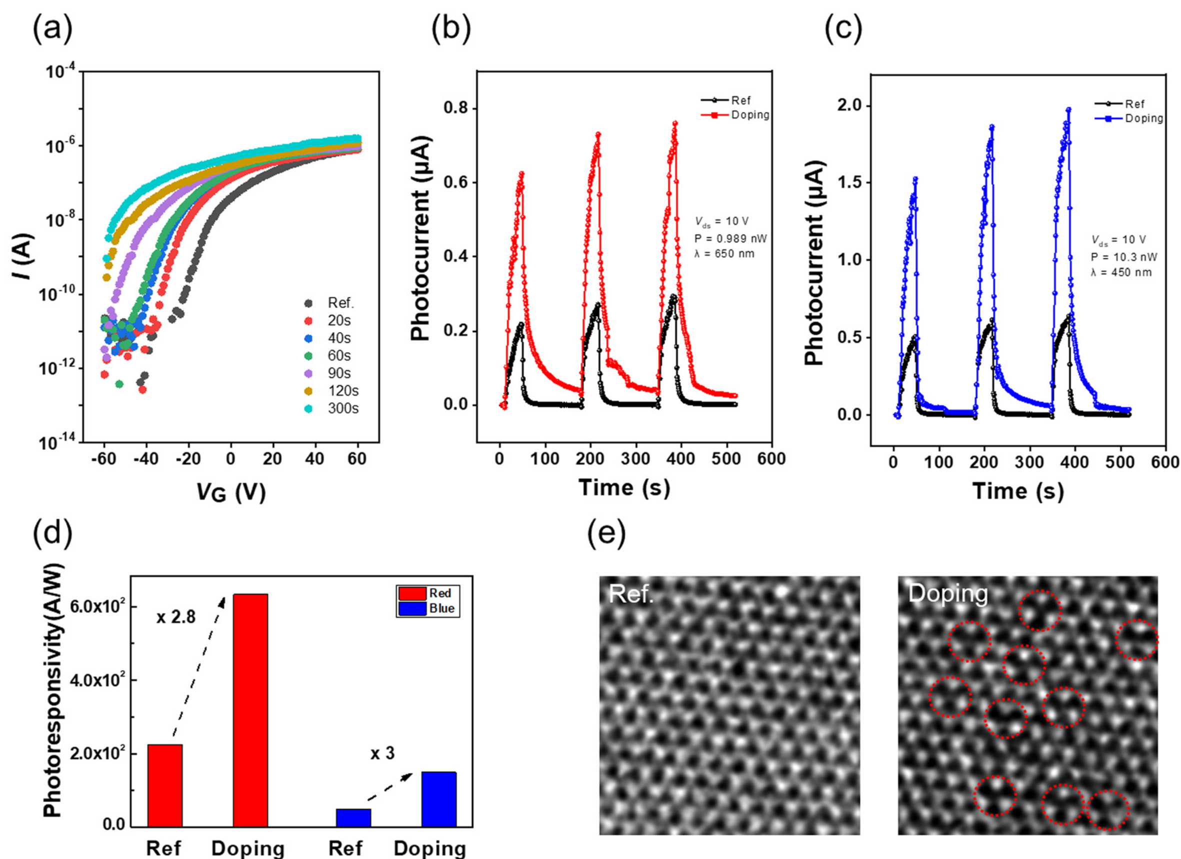

Fig. 4 Electrical and optoelectronic performance of MoS_2 before and after doping by Ar^+ ion treatment. (a) Transfer characteristics (*I*–*V* curves) of MoS_2 FETs with varying Ar^+ ion treatment duration. (b) Time-resolved photocurrent measurements under red light illumination (λ = 650 nm), showing a clear increase in photocurrent after the doping (90 s). (c) Time-resolved photocurrent measurements under blue light illumination (λ = 450 nm), also indicating a significant rise in photocurrent for doped sample (90 s) compared to the reference sample. (d) Comparison of photo-responsivity for red and blue light between reference and doped samples (90 s). (e) High-resolution STEM images of reference and doped (90 s) MoS_2 samples, where sulfur vacancies (indicated by red dashed circles) are observed in the doped sample.

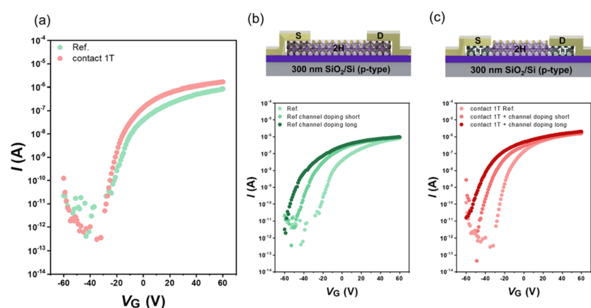

Fig. 5 Effect of 1T-phase contact on the electrical characteristics of MoS_2 FETs. (a) Transfer characteristics of a reference CVD-grown mono-layer MoS_2 back-gated FET and a device with 1T-phase converted contact regions, showing improved current levels due to reduced contact resistance. (b) Transfer curves of reference devices with and without channel doping, indicating increased current with longer doping regions. (c) Transfer curves of devices with 1T-phase contacts, showing further current enhancement when combined with channel doping (doping short: 40 s and doping long: 90 s).

increases, the change is rather modest. This is because the on-state current is a function of both carrier concentration (n) and mobility (μ). Sulfur vacancies form localized states within the bandgap that can trap charge carriers and induce hopping transport.[35] This indicates that the vacancies, while acting as donors to increase, also serve as scattering centers that limit the carrier mobility (μ). Therefore, the observed modest increase in on-state current is a result of the trade-off between the increased carrier density and the mobility limited by defect-induced hopping. Fig. 5c presents the corresponding transfer characteristics for devices with 1T-phase contacts. When channel doping is additionally applied to the 1T-contact devices, further improvement in device performance is observed. Compared to the reference, the overall enhancement in electrical behavior including higher on-current and steeper slopes-highlights the synergistic effect of metallic contact formation and doping-induced conductivity modulation. These results collectively demonstrate that converting the contact region to the 1T metallic phase is a highly effective strategy for minimizing contact resistance and improving FET performance in 2D semiconductors.

Published on 22 October 2025. Downloaded by Sungkyunkwan University on 2/3/2026 8:45:46 AM.

Fig. 6 investigates the effects of O_2 plasma-induced oxidation on MoS_2 FETs with and without Al_2O_3 encapsulation. While other van der Waals materials like h-BN can provide a more pristine, damage-free interface, our choice of ALD-Al_2O_3 is motivated by its wafer-scale uniformity, CMOS compatibility, excellent barrier properties, and its nature as a high-*k* dielectric, which is advantageous for future top-gated device applications.[36] As shown in Fig. 6a, a schematic of an unencapsulated device subjected to an O_2 plasma treatment is presented. It is well-known that oxygen plasma can actively modulate TMD properties, and recent studies have shown that mild O_2 plasma can enhance device performance through controlled oxidation or phase transitions.[36–38] In contrast, the O_2 plasma in our study is not used as a primary treatment for performance enhancement. Instead, it serves as a harsh oxidative test designed specifically to evaluate the stability of our Ar^+-treated devices and the effectiveness of the Al_2O_3 encapsulation. The corresponding transfer characteristics in Fig. 6b reveal a significant degradation in performance after oxidation, including a reduction in on-current and a noticeable shift in threshold voltage. This degradation is attributed to surface oxidation and the formation of Mo–O bonds, as supported by the XPS spectra shown in Fig. 6c. After the O_2 plasma treatment, a distinct increase in the Mo^{6+}-related peak is observed in the Mo 3d region, indicating the generation of MoO_3 species on the surface.[39] In contrast, Fig. 6d shows a device that was encapsulated with an Al_2O_3 layer after the primary Ar^+ ion treatment. As shown in Fig. 6e, the encapsulated device demonstrates dramatically improved stability under harsh O_2 plasma conditions compared to the unencapsulated device (Fig. 6b). The minor negative shift in the threshold voltage observed after encapsulation is consistent with previous reports, which attribute to n-doping effects in ALD Al_2O_3 to defects such as fixed positive charges, oxygen vacancies, or carbon impurities within the oxide.[40–42] However, since excellent characteristics such as a high on/off ratio were maintained, this can be considered as a manageable electrical effect rather than significant device degradation. Crucially, this result proves that the Al_2O_3 layer encapsulation successfully fulfilled its function as an excellent protective barrier against oxidation. The XPS spectra in Fig. 6f confirms this observation: the Mo^{6+} peak is significantly suppressed in the encapsulated sample, suggesting that the Al_2O_3 layer effectively blocks oxygen diffusion and protects the MoS_2 surface from oxidation. Importantly, this protective effect of Al_2O_3 encapsulation is also evident under milder yet realistic conditions such as ambient air exposure. As shown in Fig. S3, Ar^+ ion treated MoS_2 devices without encapsulation undergo noticeable electrical degradation after just 5 days in air, whereas the devices with Al_2O_3 encapsulation retain their performance, confirming its effectiveness in suppressing slow oxidative degradation during storage or operation in air. These results highlight the critical role of surface passivation in preserving the electrical properties of 2D semiconductors during the processing.

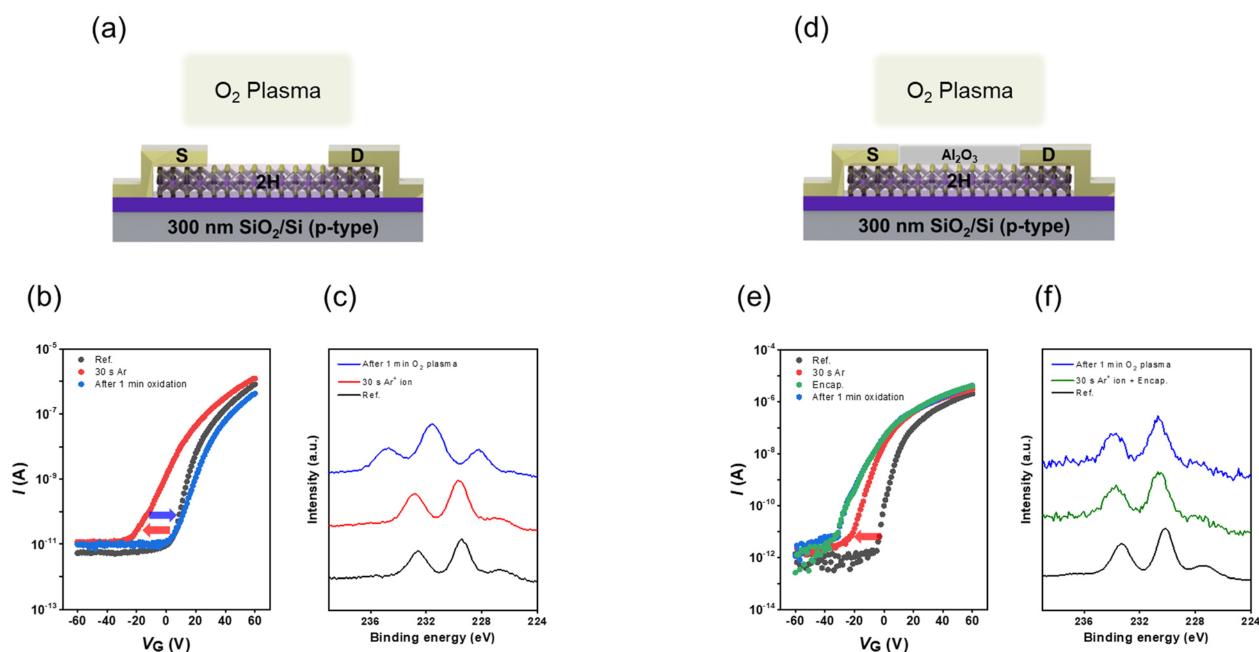

Fig. 6 Effects of O_2 plasma oxidation on MoS_2 FETs with and without Al_2O_3 encapsulation. (a) O_2 plasma treatment. (b) Transfer characteristics showing reduced on-current and threshold voltage shift after oxidation. (c) Mo 3d XPS spectra of reference, and Ar^+ ion pretreated and O_2 plasma oxidized samples, showing increased Mo^{6+} peak due to surface oxidation. (d) Schematic of a MoS_2 FET with Al_2O_3 encapsulation during an O_2 plasma exposure. (e) Transfer characteristics of the encapsulated device showing better current retention and minimized degradation. (f) Mo 3d XPS spectra of the encapsulated sample, where Mo^{6+} peak growth is significantly suppressed, indicating effective protection by Al_2O_3.

 This journal is © The Royal Society of Chemistry 2025

Published on 22 October 2025. Downloaded by Sungkyunkwan University on 2/3/2026 8:45:46 AM.

Experimental

Preparation of CVD MoS_2 and device fabrication

Monolayer MoS_2 samples (1 cm × 1 cm) were purchased from 6 Carbon Co., Ltd. For the transfer process, the CVD-grown MoS_2 was first coated with poly(methyl methacrylate) (PMMA). A thermal release tape (TRT) was then attached to the PMMA layer. The entire stack was submerged in water to delaminate the TRT/PMMA/MoS_2 film from the original growth substrate. Subsequently, the film was transferred onto a new target substrate (a 300 nm-thick SiO_2/p^{++}-doped Si). The TRT was removed by applying heat, and the PMMA support layer was then dissolved using acetone and ethanol. After transfer, source and drain electrodes were patterned by photolithography and deposited using electron-beam evaporation of chromium (5 nm) and gold (50 nm). The resulting device structure was used for subsequent doping and electrical characterization.

Ar^+ ion treatment

The controllable n-type doping was performed using a 3-grid inductively coupled plasma (ICP) ion beam system (a schematic is shown in Fig. 1a), which is composed of three grids.[43] A positive DC voltage is applied to the 1st grid to accelerate Ar^+ ions from the plasma source through the grid holes, and a negative DC voltage is typically applied to the 2nd grid to form a parallel ion beam. The 3rd grid and the sample holder are grounded. In this study, the ion energy was controlled by applying 25 V to the first grid, while no voltage was applied to the second grid. This setup provides a low-energy Ar^+ ion bombardment of ∼25 eV sufficient for the selective removal of only sulfur atoms without causing significant damage to the underlying MoS_2 film.

O_2 plasma oxidation treatment

O_2 plasma oxidation was conducted using a remote inductively coupled plasma (ICP) system equipped with dual crossed-hole grids to eliminate energetic ion bombardment on the substrate. The O_2 plasma was generated at a pressure of 100 mTorr and an RF power of 200 W. All plasma treatments were carried out at room temperature without external substrate heating. The process was used to evaluate the oxidation stability of MoS_2 surfaces with and without Al_2O_3 encapsulation, as described in the main text.

Atomic layer deposition of Al_2O_3 encapsulation layer

This passivation layer was deposited onto the devices after the primary Ar^+ ion treatment process to evaluate its protective effect during subsequent stability tests. ALD-Al_2O_3 films were deposited using trimethylaluminum (TMA) precursor and H_2O reactant, serving as passivation layers for the channel in bottom-gate FETs. Based on previous studies, the purging time was reduced to improve film coverage on the MoS_2 surface by suppressing precursor desorption.[44] Each ALD cycle consisted of TMA/N_2/H_2O/N_2 injections of 1 s/2 s/5 s/3 s, resulting in a deposition rate of 1.4 Å per cycle. The final film thickness was ∼10 nm, measured on HF-cleaned and co-processed Si substrates using a spectroscopic ellipsometer (SE MG-1000UZ, located at the MEMS Sensor Platform Center of Sungkyunkwan University, NANO-VIEW).

Characterization methods

Raman and photoluminescence (PL) spectra of the MoS_2 samples were measured using a confocal Raman microscope (WITec Alpha 300 M$^+$) with a 532 nm excitation laser. X-ray photoelectron spectroscopy (XPS, MultiLab 2000, Thermo VG, Mg Kα source) was employed to analyze the chemical states and composition, with the binding energy calibrated to the C 1s peak at 284.8 eV. HR-TEM (HR-STEM, JEOL JEM-ARM200F) was used to observe atomic-scale structural changes after plasma treatment. The electrical measurements of MoS_2 field-effect transistors were carried out using a semiconductor parameter analyzer (Keysight B2912A) in a vacuum probe station. Transfer curves were used to extract the field-effect mobility, and threshold voltage shifts were monitored under varying doping conditions. Photoresponse measurements were performed under red (650 nm) and blue (450 nm) light illumination, and photoresponsivity was calculated as $R = I_{photo}/P_{led}$.

Conclusions

In this study, we demonstrated a controllable and damage-free approach for n-type doping and phase transition in large-area CVD-grown MoS_2 by engineering sulfur vacancies using a precisely modulated Ar^+ ion treatment. By precisely tuning the ion energy and exposure time, we achieved selective formation of top-layer sulfur vacancies that act as electron donors, thereby enhancing n-type conductivity. With extended Ar^+ ion treatment duration, a structural phase transition from semiconducting 2H to metallic 1T was also realized, as confirmed by Raman, PL, and XPS analyses. The resulting doped MoS_2 devices exhibited improved electrical and optoelectronic performance, including enhanced on-current, photoresponsivity, and electron mobility. Furthermore, we demonstrated that contact engineering through selective 1T-phase conversion at source/drain regions significantly reduces contact resistance and enables further device performance enhancement, especially when combined with channel doping. In addition, the use of Al_2O_3 encapsulation was shown to effectively prevent surface oxidation during an O_2 plasma exposure, preserving device integrity and electrical stability. These results demonstrate that plasma-assisted defect and phase engineering is a practical and scalable approach to tailoring the electronic properties of two-dimensional semiconductors, offering promising potential for future applications in nanoelectronics and optoelectronics.

Author contributions

J. Kim and J. Kang: methodology, investigation, visualization, writing. H. Han, S. Jeong, S. Kim, H. Lee: investigation, data

Published on 22 October 2025. Downloaded by Sungkyunkwan University on 2/3/2026 8:45:46 AM.

curation. H. Kim: conceptualization, resources. Y. Kim and G. Yeom: conceptualization, resources, supervision.

Conflicts of interest

There are no conflicts to declare.

Data availability

The data supporting the findings of this study are available within the article and its supplementary information (SI). See DOI: https://doi.org/10.1039/d5nr03806e.

Acknowledgements

This work was supported by the Technology Innovation Program (public-private joint investment semiconductor R&D program (K-CHIPS) to foster high-quality human resources) (RS-2023-00235484, "Development of High Quality MX2 Materials and Processes through *in situ* Defect Analysis") funded by the Ministry of Trade, Industry & Energy (MOTIE, Korea)(1415187770) and a National Research Foundation of Korea (NRF) grant funded by the Korea government (MSIT) (No. 2022R1A2C2091660).

References

1 B. Radisavljevic, A. Radenovic, J. Brivio, V. Giacometti and A. Kis, *Nat. Nanotechnol.*, 2011, **6**, 147–150.
2 O. Lopez-Sanchez, D. Lembke, M. Kayci, A. Radenovic and A. Kis, *Nat. Nanotechnol.*, 2013, **8**, 497–501.
3 A. Splendiani, L. Sun, Y. Zhang, T. Li, J. Kim, C. Y. Chim, G. Galli and F. Wang, *Nano Lett.*, 2010, **10**, 1271–1275.
4 K. F. Mak, C. Lee, J. Hone, J. Shan and T. F. Heinz, *Phys. Rev. Lett.*, 2010, **105**, 136805.
5 D. Dumcenco, D. Ovchinnikov, K. Marinov, P. Lazic, M. Gibertini, N. Marzari, O. L. Sanchez, Y. C. Kung, D. Krasnozhon, M. Chen, *et al.*, *ACS Nano*, 2015, **9**, 4611–4620.
6 Y.-H. Lee, X.-Q. Zhang, W. Zhang, M.-T. Chang, C.-T. Lin, K.-D. Chang, Y.-C. Yu, J. T.-W. Wang, C.-S. Chang, L.-J. Li, *et al.*, *arXiv*, 2012, preprint, arXiv:1202.5458, DOI: 10.48550/arXiv.1202.5458.
7 K.-Y. Yang, M. Li, L. Bai, X. Zhang, Y. Li and Y. Zhang, *Sci. Rep.*, 2023, **13**, 8378.
8 A. Azcatl, X. Qin, A. Prakash, C. Zhang, L. Cheng, Q. Wang, J. Kim, J. Appenzeller, S. K. Fullerton-Shirey, R. M. Wallace, *et al.*, *Nano Lett.*, 2016, **16**, 5437–5443.
9 P. Tan, M. Wang, Y. Liang, J. Liu and F. Pan, *Nanoscale*, 2021, **13**, 15278–15284.
10 K. H. Kim, D.-H. Kang, M. Park, Y. Kim, J.-S. Kim, S. Yoo, H. Chang and J. Kim, *J. Mater. Chem. C*, 2020, **8**, 1846–1851.
11 M. Telkhozhayeva and O. Girshevitz, *Adv. Funct. Mater.*, 2024, **34**, 2404615.
12 H. Qiu, L. Pan, Z. Yao, J. Li, Y. Shi and X. Wang, *Nat. Commun.*, 2013, **4**, 2642.
13 J. Hong, Z. Hu, M. Probert, K. Li, D. Lv, X. Yang, L. Gu, N. Mao, Q. Feng, L. Xie, *et al.*, *Nat. Commun.*, 2015, **6**, 6293.
14 M. Rajput, S. Barik, K. V. Kannan, R. Chauhan, R. K. Jha and A. Srivastava, *Commun. Mater.*, 2024, **5**, 190.
15 Y. Zhao, Z. Wang, Z. Zhang, J. Qiu, X. Wang and Y. Liu, *Nat. Commun.*, 2023, **14**, 44.
16 J. Hong, Z. Hu, M. Probert, K. Li, D. Lv, X. Yang, L. Gu, N. Mao, Q. Feng, L. Xie, *et al.*, *Nat. Commun.*, 2015, **6**, 6293.
17 M. Kang, Y. J. Kim, D. Jeong, H. J. Park, S. Lee, S.-H. Lee and W. Choi, *ACS Appl. Mater. Interfaces*, 2024, **16**, 43849–43859.
18 M. Liu, L. Sun, K. Xu, Y. Li, W. Xu and J. He, *Small*, 2017, **13**, 1602967.
19 S.-S. Chee, J. Y. Oh, K. Kim and C.-H. Lee, *Nanoscale*, 2017, **9**, 9333–9339.
20 K. S. Kim, H. B. Lee, Y. Lee, Y. Kim and S. Cho, *ACS Appl. Electron. Mater.*, 2022, **4**, 3794–3800.
21 B. Chakraborty, A. Bera, D. V. S. Muthu, S. Bhowmick, U. V. Waghmare and A. K. Sood, *Phys. Rev. B:Condens. Matter Mater. Phys.*, 2012, **85**, 16140.
22 Y. Yao, K. Ao, P. Lv and Q. Wei, *Nanomaterials*, 2019, **9**, 844.
23 J. Jung, H. Y. Bark, D. Byun, C. Lee and D.-H. Cho, *2D Mater.*, 2019, **6**, 025024.
24 B. Chakraborty, A. Bera, D. V. S. Muthu, S. Bhowmick, U. V. Waghmare and A. K. Sood, *Phys. Rev. B:Condens. Matter Mater. Phys.*, 2012, **85**, 161403.
25 M. F. Hossen, S. Shendokar, M. A. R. Khan and S. Aravamudhan, *Nano Sel.*, 2024, **6**, e202400103.
26 S. Mouri, Y. Miyauchi and K. Matsuda, *Nano Lett.*, 2013, **13**, 5944–5948.
27 L. Yang, K. Majumdar, H. Liu, Y. Du, H. Wu, M. Hatzistergos, P. Y. Hung, R. Tieckelmann, W. Tsai, C. Hobbs and P. D. Ye, *Nano Lett.*, 2014, **14**, 6275–6280.
28 K. S. Kim, K. H. Kim, Y. Nam, J. Jeon, S. Y. Yim, E. Singh, J. Y. Lee, S. J. Lee, Y. S. Jung, G. Y. Yeom and D. W. Kim, *ACS Appl. Mater. Interfaces*, 2017, **9**, 11967–11976.
29 G. Eda, H. Yamaguchi, D. Voiry, T. Fujita, M. Chen and M. Chhowalla, *Nano Lett.*, 2011, **11**, 5111–5116.
30 K. S. Kim, K. H. Kim, Y. Nam, J. Jeon, S. Yim, E. Singh, J. Y. Lee, S. J. Lee, Y. S. Jung, G. Y. Yeom and D. W. Kim, *ACS Appl. Mater. Interfaces*, 2017, **9**, 11967–11976.
31 Q. Tang, *J. Mater. Chem. C*, 2018, **6**, 9561–9568.
32 S. Park, A. T. Garcia-Esparza, H. Abroshan, B. Abraham, J. Vinson, A. Gallo, D. Nordlund, J. Park, T. R. Kim, L. Vallez, R. Alonso-Mori, D. Sokaras and X. Zheng, *Adv. Sci.*, 2021, **8**, 2002768.
33 N. Luo, C. Chen, D. Yang, W. Hu and F. Dong, *Appl. Catal., B*, 2021, **299**, 120664.
34 I. H. Abidi, A. Bhoriya, P. Vashishtha, S. P. Giridhar, E. L. H. Mayes, M. Sehrawat, A. K. Verma, V. Aggarwal, T. Gupta, H. K. Singh, T. Ahmed, N. D. Sharma and S. Walia, *Nanoscale*, 2024, **16**, 19834.

This journal is © The Royal Society of Chemistry 2025

35 H. Qiu, T. Xu, Z. Wang, W. Ren, H. Nan, Z. Ni, Q. Chen, S. Yuan, F. Miao, F. Song, G. Long, Y. Shi, L. Sun, J. Wang and X. Wang, *Nat. Commun.*, 2013, **4**, 2642.

36 Z. Cheng, S. He, S. Zhang, S. Duan, M. Wang, Z. Liu, R. Zhang, W. Qiang, X. Zhang and M. Xia, *Nano Res.*, 2024, **17**, 3253–3260.

37 Z. Cheng, S. He, X. Han, X. Zhang, L. Chen, S. Duan, S. Zhang and M. Xia, *J. Mater. Chem. C*, 2024, **12**, 2794–2802.

38 S. He, Z. Cheng, S. Duan, X. Zhang, L. Chen, Q. Lou, Z. Wu, S. Zhang, S. Zhang and M. Xia, *J. Mater. Chem. C*, 2025, **13**, 5746–5753.

39 Y.-T. Ho, C.-H. Ma, T.-T. Luong, L.-L. Wei, T.-C. Yen, W.-T. Hsu, W.-H. Chang, Y.-C. Chu, Y.-Y. Tu, K. P. Pande and E. Y. Chang, *Phys. Status Solidi RRL*, 2015, **9**, 187–191.

40 A. Leonhardt, D. Chiappe, V. V. Afanas'ev, S. El Kazzi, I. Shlyakhov, T. Conard, A. Franquet, C. Huyghebaert and S. de Gendt, *ACS Appl. Mater. Interfaces*, 2019, **11**, 42697–42707.

41 A. Valsaraj, J. Chang, A. Rai, L. F. Register and S. K. Banerjee, *2D Mater.*, 2015, **2**, 045009.

42 J. Na, M.-K. Joo, M. Shin, J. Huh, J.-S. Kim, M. Piao, J.-E. Jin, H.-K. Jang, H. J. Choi, J. H. Shim and G.-T. Kim, *Nanoscale*, 2014, **6**, 433–441.

43 D. S. Kim, H. I. Kwon, Y. J. Jang, G. C. Kim, H. S. Gil, D. W. Kim, B. H. Jeong and G. Y. Yeom, *Appl. Surf. Sci.*, 2024, **670**, 160570.

44 Y. S. Lin, P. H. Cheng, K. W. Huang, H. C. Lin and M. J. Chen, *Appl. Surf. Sci.*, 2018, **443**, 421–428.

Published on 22 October 2025. Downloaded by Sungkyunkwan University on 2/3/2026 8:45:46 AM.